

AN AB INITIO APPROACH TO THE SOLAR CORONAL HEATING PROBLEM

B.V. GUDIKSEN AND Å. NORDLUND

Draft version November 7, 2018

ABSTRACT

We present an *ab initio* approach to the solar coronal heating problem by modelling a small part of the solar corona in a computational box using a 3D MHD code including realistic physics. The observed solar granular velocity pattern and its amplitude and vorticity power spectra, as reproduced by a weighted Voronoi tessellation method, are used as a boundary condition that generates a Poynting flux in the presence of a magnetic field. The initial magnetic field is a potential extrapolation of a SOHO/MDI high resolution magnetogram, and a standard stratified atmosphere is used as a thermal initial condition. Except for the chromospheric temperature structure, which is kept fixed, the initial conditions are quickly forgotten because the included Spitzer conductivity and radiative cooling function have typical timescales much shorter than the time span of the simulation. After a short initial start up period, the magnetic field is able to dissipate $3 - 4 \times 10^6 \text{ ergs cm}^{-2} \text{ s}^{-1}$ in a highly intermittent corona, maintaining an average temperature of $\sim 10^6 \text{ K}$, at coronal density values for which emulated images of the Transition Region And Coronal Explorer (TRACE) 171 and 195 Å pass bands reproduce observed photon count rates.

Subject headings: Sun: corona – Sun: magnetic fields – MHD

1. INTRODUCTION

The heating mechanism at work in the solar corona has puzzled researchers for more than six decades. Several heating mechanisms have been proposed. One of the earliest models involved accretion of interstellar matter coupled with convection in the chromosphere (Bondi et al. 1947), but with improved measurements two main groups of heating models emerged: Wave (AC) heating and electric current (DC) heating. These mechanisms move energy from the photospheric kinetic energy reservoir to the internal heat reservoir in the corona through the magnetic field. AC heating (already proposed by Alfvén 1947) depends on the magnetic field being moved around in the solar photosphere faster than the disturbances can propagate through the whole magnetic loop, i.e. faster than the Alfvén crossing time. Only torsional Alfvén waves can reach the corona, while magneto-sonic wave modes are diffracted and dissipated due to the strong wave speed gradient in the chromosphere/transition region. Waves have been detected both in the near Sun corona (see for instance Aschwanden 1987; Ofman & Davila 1997) as well as in the solar wind by a number of spacecrafts such as the Helios satellites (Neubauer & Musmann 1977) so there is firm evidence for their existence, but not of their ability to supply enough heat. Alfvén waves do not easily dissipate in the corona in the absence of phase mixing (Heyvaerts & Priest 1983) or resonant absorption (Davila 1987), which require strong phase speed gradients to be efficient.

DC heating relies on motions in the photosphere that change on time scales longer than Alfvén crossing times, making the magnetic field remain close to an equilibrium state. The DC heating mechanism dissipates energy through conventional Joule heating (proposed by Parker 1972), or reconnection heating (proposed by Glencross et al. 1974, based on X-ray observations) dissipated through flares of all sizes,

including nano-flares, or through a hierarchy of current sheets that may encompass both of the above processes (Galsgaard & Nordlund 1996). Until recently, nano-flares appeared to be the most promising candidate, but it now seems that the energy dissipated in the observed flare distribution, extrapolated to a cut-off at nano-flare energies, is too small (Aschwanden et al. 2000; Parnell & Jupp 2000; Aschwanden & Parnell 2002; Aschwanden & Charbonneau 2002). DC heating has received considerable attention since it was proposed some thirty years ago (e.g. Parker 1972, 1983; Sturrock & Uchida 1981; van Ballegoijen 1986; Mikic et al. 1989; Heyvaerts & Priest 1992; Longcope & Sudan 1994; Galsgaard & Nordlund 1996; Hendrix et al. 1996; Gomez et al. 2000, to mention just a few). It has been established that the DC heating mechanism is feasible, but not to what extent it can provide enough energy to heat the solar corona.

The main problem in modelling solar dissipative processes is the length scales involved. The dissipative length scale is of the order of 1 m for e.g. a flare with a time scale of the order 100 s, while the large scale magnetic field distribution has a scale of many Mm, making fully resolved 3D simulations of such processes practically impossible. However, the theoretical results of Parker (1979) and the numerical results of Galsgaard & Nordlund (1996) and Hendrix et al. (1996) have shown that it is not necessary to resolve the dissipative length scales because the total dissipation only depends very weakly on the resolution, and if anything increases with increasing resolution. Results from low resolution modelling of dissipative processes may thus be used to obtain estimates, or at least establish *lower* limits on the dissipated energy. This provides the basis for trying to create numerical *ab initio* simulations of the solar corona, with essentially no free parameters. As discussed in more detail below, the initial and boundary conditions that we use are *minimal assumptions*, in the sense that including more detailed conditions would pro-

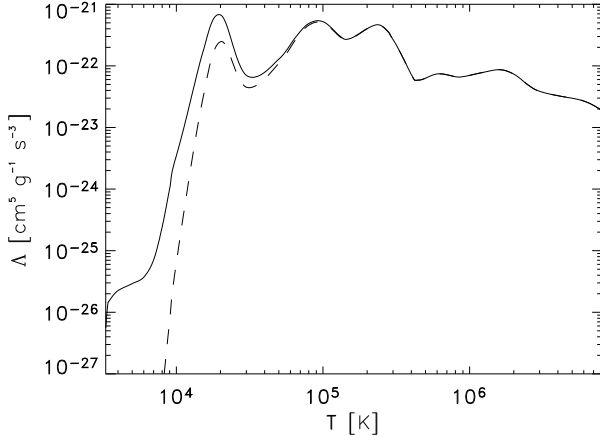


FIG. 1.— Radiative cooling function (full) and implemented cooling function (dashed) with quenched cooling in the photospheric and chromospheric temperature regimes

duce more heating. This allows us to give a firm answer to whether DC heating can provide the energy required and thus which heating mechanism is the principal one in the solar corona.

Initial results of this effort were presented in Gudiksen & Nordlund (2002) and here we present further developments including a realistic photospheric velocity driver and a non uniform mesh, making it possible to resolve the density drop in the transition region and expand the simulated volume.

2. MODEL

We solve the fully compressible MHD equations on a non-uniform staggered mesh, in the form

$$\frac{\partial \rho}{\partial t} = -\vec{\nabla} \cdot \rho \vec{u} \quad (1)$$

$$\frac{\partial \rho \vec{u}}{\partial t} = -\vec{\nabla} \cdot (\rho \vec{u} \vec{u} - \tau) - \vec{\nabla} P + \vec{J} \times \vec{B} + \rho \vec{g} \quad (2)$$

$$\mu \vec{J} = \vec{\nabla} \times \vec{B} \quad (3)$$

$$\vec{E} = \eta \vec{J} - \vec{u} \times \vec{B} \quad (4)$$

$$\frac{\partial \vec{B}}{\partial t} = -\vec{\nabla} \times \vec{E} \quad (5)$$

$$\frac{\partial e}{\partial t} = -\vec{\nabla} \cdot e \vec{u} - P \vec{\nabla} \cdot \vec{u} - \vec{\nabla} \cdot \vec{F}_{\text{Spitzer}} + Q_{\text{visc}} + Q_{\text{Joule}} - n_{\text{ion}} n_e \Lambda, \quad (6)$$

where ρ is the mass density, \vec{u} the velocity vector, τ the viscous stress tensor, P the gas pressure, \vec{J} the electric current density, \vec{B} the magnetic flux density, \vec{g} the gravitational acceleration, μ the vacuum permeability, \vec{E} the electric field strength, η the magnetic diffusivity, e the internal energy per unit volume, \vec{F}_{Spitzer} is the energy flux due to the Spitzer conductivity (Spitzer 1956) along the magnetic field, Q_{visc} is the viscous heating, Q_{Joule} is the Joule heating, and Λ is the cooling function for the optically thin coronal plasma with n_{ion} and n_e being the number density of ions and electrons.

The code is explicit and, because of the staggered mesh method, conserves the magnetic divergence to machine precision. The staggered mesh method means that the

physical variables are not aligned in space. This is an advantage for the derivative operators, but has the downside that when physical variables at different locations are involved interpolation is needed to realign the variables. The code uses 6'th order derivative operators and 5'th order interpolation operators, together with a 3'rd order Runge-Kutta time stepping method with variable time step. The code has been extensively subjected to several standard tests as well as used in several physical regimes, for instance 3-D turbulence and magneto-convection (Nordlund et al. 1994), magnetic dissipation (Galsgaard & Nordlund 1996), buoyant magnetic flux tubes (Dorch & Nordlund 1998), emergence of flux ropes through the solar convection zone (Dorch et al. 1999), and supersonic MHD-turbulence (Padoan & Nordlund 1999).

The computational box of $60 \times 60 \times 37 \text{ Mm}^3$ is resolved on a grid of 150^3 grid points where the vertical scale is non-uniform. The vertical axis starts at the photosphere, with high resolution ($\sim 0.15 \text{ Mm}$) in order to resolve the small pressure scale height in the photosphere and chromosphere. Above the transition region the vertical resolution gradually approaches 0.25 Mm .

2.1. Radiative cooling

The cooling function includes the most important transitions for H, He, C, O, Ne, Fe and bremsstrahlung, with a cut off at low temperatures to avoid catastrophic cooling in the chromosphere (see Fig. 1). The cooling function is based on the ionisation and recombination rates given by Arnaud & Rothenflug (1985); Shull & van Steenberg (1982) and using the collisional excitation rates found through the HAO-DIAPER Atom data package (Judge & Meisner 1994). The ions are treated by assuming ionisation equilibrium making it possible to derive radiative losses as a function of electron temperature.

Further down in the atmosphere, where the radiation is optically thick for at least some wavelengths, the cooling processes cannot be treated with a simple cooling function. The cooling function shown in Fig. 1(full) uses a cutoff proportional to $\exp(-\tau)$ with the optical depth $\tau \propto P_{\text{gas}}$. In this simulation, the lower part of the chromosphere and the photosphere are instead kept near a fixed average temperature profile using a Newtonian cooling mechanism that forces the local temperature towards a preset function of height on a timescale of about 0.1 s in the photosphere. The time scale increases with decreasing density as $\rho^{-1.67}$, and the effect thus becomes negligible in the corona.

2.2. Boundary conditions

The vertical boundary conditions are handled by using ghost zones, while the box is periodic in the horizontal directions. The density is extrapolated into the ghost zones, and to prevent heat from leaking into or out of the box, the temperature gradient is set to zero at the upper boundary. The upper boundary is relaxed towards the average temperature at the upper boundary with a typical time scale of about 30 s . The vertical velocity is zero on the boundaries, while the horizontal velocity on the lower boundary is set by a driver (See §2.3). At the upper boundary the vertical gradient of the horizon-

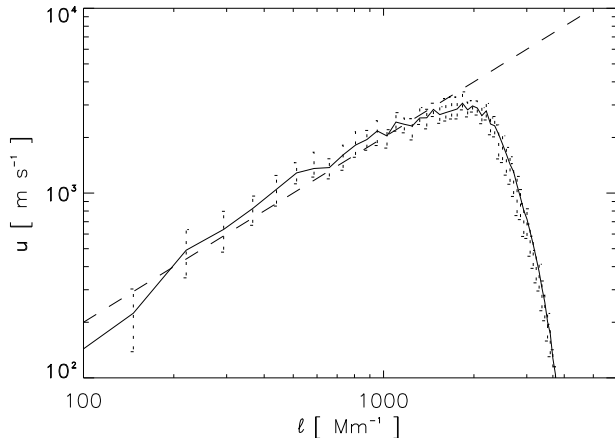


FIG. 2.— Velocity amplitude versus spherical harmonic wavenumber for the three layer granulation model (full) with the error bars showing maximum deviation through a period of 1 hour. The dashed line shows $u \propto k$.

tal velocity is set to zero and we use a potential field extrapolation for the magnetic field in the ghost zones.

2.3. The Voronoi tessellation driver

The solar photospheric velocity field is characterised by granular structures with a range of sizes, from granules with a typical size of ~ 1 Mm to super-granules of size ~ 20 – 30 Mm and even bigger giant cells (Simon & Weiss 1968; Hathaway et al. 2000). These structures have typical velocities that scale with wavenumber roughly as $u \propto k$ and have turnover times of the order $\tau \propto k^{-2}$, all the way from beyond super-granular scales to the velocity maximum at granular scales (Stein & Nordlund 1998; Hathaway et al. 2000; Shine et al. 2000). The velocity field injects energy into the magnetic field through a Poynting flux, making a realistic reproduction important.

Our goal was to create a driver that would match these statistical features of the solar velocity spectrum, as well as the geometrical features of the granular pattern. The velocity driver is partially based on the theory of *Voronoi tessellation* (see for instance Okabe et al. 1992) specifically multiplicatively weighted Voronoi tessellation, inspired by Schrijver et al. (1997a) who showed that this method gives a good fit to observations of the granulation pattern. The theory applied to this case provides a way to split a 2-D surface into tiles, each representing a granule. To do this one has to choose a number of generator points, each with a weight w_i (where i represents a specific tile) positioned at \vec{x}_i . Tile i then occupies an area where the following inequality is satisfied,

$$\frac{w_i}{|\vec{x} - \vec{x}_i|} \geq \frac{w_j}{|\vec{x} - \vec{x}_j|} \quad \text{for all } j \neq i. \quad (7)$$

To include the intergranular lanes, we increased the complexity of Eq. 7,

$$\frac{w_i(1 - l_{ig})}{|\vec{x} - \vec{x}_i|} \geq \frac{w_j}{|\vec{x} - \vec{x}_j|} < \frac{w_i(1 + l_{ig})}{|\vec{x} - \vec{x}_i|}. \quad (8)$$

When both conditions are true \vec{x} is in an intergranular lane, and where only the left part of the inequality is true \vec{x} is in granule i . l_{ig} is a number between zero

and one and can be adjusted to make the intergranular area roughly 33-45% of the total area (Stein & Nordlund 1998) based on velocity maps. The relative area of the intergranular lanes can be estimated by assuming perfectly round granules,

$$\frac{A_{ig}}{A_{tot}} = 2l_{ig} \frac{(1 - l_{ig})}{(1 + l_{ig})}. \quad (9)$$

2.3.1. The initial tessellation

If the generator points were placed randomly there would be both unusually large and unusually small granules generated, because the density of generator points would be low in some places and high in others. Since observed granules are rather uniform in size, only a certain range of sizes of fully grown granules can be accepted. This places restrictions on the placement of the generator points. The tessellation is built up by keeping a list of the weights at each position, independent of whether it is in an intergranular lane or not, updating the list as more granules are placed. In this way a weight function with a value at each position is generated,

$$\mathcal{W}(\vec{x}) = \frac{w_i}{|\vec{x} - \vec{x}_i|} \quad \text{where} \quad \frac{w_i}{|\vec{x} - \vec{x}_i|} \geq \frac{w_j}{|\vec{x} - \vec{x}_j|} \quad \text{for all } j \neq i. \quad (10)$$

To generate a new granule, its generator point is placed where the weight function has a value lower than a certain threshold $\mathcal{W}_{\text{thresh}}$. This allows more generator points to be placed only until the weight function is above the threshold at all positions. By choosing an appropriate threshold carefully the density of generator points is such that granules of the right size are created.

The velocity vector points radially away from the generator points inside the granules, and along the granular boundaries in the intergranular lanes. The horizontal velocity profile inside meso-granules was modelled by Simon & Weiss (1989) by fitting a simple model to observations done with the SOUP filter on Spacelab 2. The horizontal velocity profiles were successfully fitted with a radial velocity profile of the form $\vec{v}_h(r) = r \exp(-(r/r_0)^2)$. We found a better fit to the solar velocity power spectrum by using $\vec{v}_h(r) = r^2 \exp(-(r/r_0)^2)$, giving a flatter profile in the centre of the granules. In the intergranular lanes the velocity is a sum of the velocity of the two granules adjacent to the intergranular lane. Initially this creates stagnation points in the intergranular lanes, on lines connecting the generator points, but such stagnation points disappear when multiple velocity fields are added (see §2.3.2).

2.3.2. Time evolution

The tessellation is made time dependent by making the weights of the generator points time dependent. We have chosen to give the weights of the generator points a time dependence specified by

$$w_i(t) = W_i \exp\left(-\left(\frac{t - t_{0,i}}{\tau_i}\right)^q\right), \quad (11)$$

where W_i is a constant giving the maximum weight, $t_{0,i}$ is the time of maximum weight, and q is an even integer, indirectly controlling the growth time of the granule. We

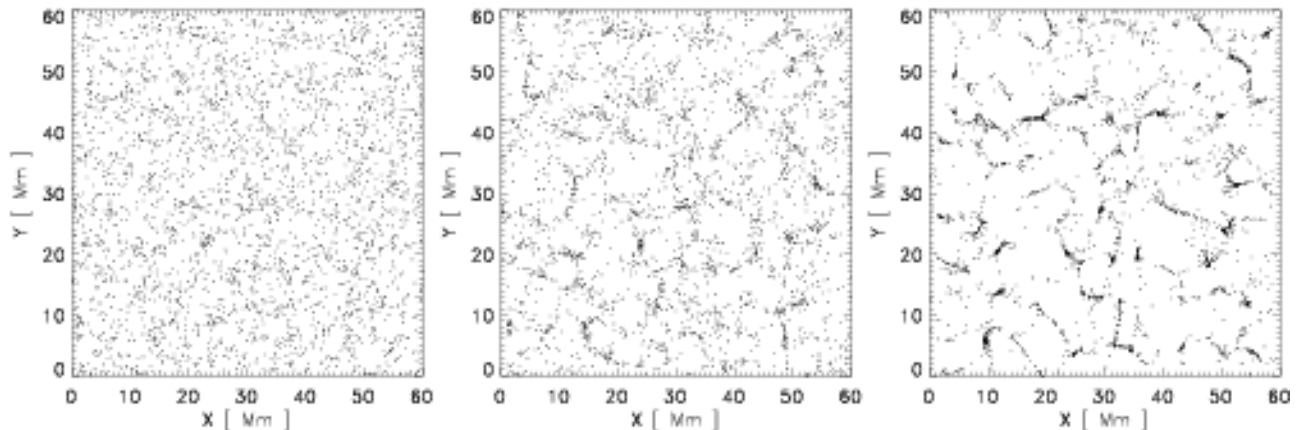


FIG. 3.— Three snapshots of 3000 corks released in the simulated velocity field, without magnetic velocity quenching, at $t = 0$ min (left), $t = 15$ min (middle), and $t = 45$ min (right)

bring the granule to life when $w_i/dx > \mathcal{W}_{\text{thresh}}$ where dx is the grid resolution, which effectively sets $t_{0,i}$ when W_i is chosen. When $t > t_{0,i}$ the granule is decaying and it is removed when $w_i/dx < \mathcal{W}_{\text{thresh}}$.

When the weight function $\mathcal{W}(\vec{x})$ falls below the threshold in a large connected region, each new granule covers only a small area, causing many small granules to appear, thus making the area crowded with small granules of approximately equal size. This problem is solved by creating a binary function $\mathcal{A}(\vec{x}, t)$, which is set to one within 80 % of the expected radius for granule i at $t = t_{0,i}$ as long as $t \leq t_{0,i}$ and otherwise zero. This region of avoidance keeps new granules from being formed in the immediate vicinity of other newly formed granules. Therefore there are two criteria a new generator point (n) must fulfil when it is generated, in order to be part of the tessellation,

$$\begin{aligned} \mathcal{W}(\vec{x}_n, t) &< W_{\text{thresh}} \\ \mathcal{A}(\vec{x}_n, t) &= 0. \end{aligned}$$

This ensures that there is room for a new granule and avoids overpopulation of new granules later when the granules are growing. At the same time the weight function evolves such that it makes new granules appear only in intergranular lanes, because this is the location where the weight function first drops below the threshold.

In order to create the velocity-scale relation of the Sun, several granular patterns with different scales must be superposed. This involves creating a number of independent granulation patterns with different typical scales as described above and adding the velocities. We have chosen three layers, with typical granular radii of 1.3, 2.5, and 5.1 Mm respectively, with velocities and lifetimes following the observed scaling relations. This choice corresponds to sizes ranging from those of large granules to the size of mesogranules, and produces on average 880, 280 and 80 granules respectively, in the three size groups. The smallest scale is set by the resolution and the largest scale is set by the box size used in the simulation.

Creating the velocity field in this way makes the velocity field ordered on many scales, but also makes it too laminar. The vorticity spectrum from the Voronoi driver is too weak compared to the simulations of Stein & Nordlund (1998). This has been corrected by

using a Helmholtz projection to separate the rotational and irrotational part of the velocity field and then amplifying the rotational part to the same level as in the simulations by Stein & Nordlund (1998).

The velocity is quenched by a factor

$$f_{\text{quench}} = \frac{1 + \beta^{-2}}{1 + 3\beta^{-2}}, \quad (12)$$

depending on the plasma $\beta = P_{\text{gas}}/P_{\text{Mag}}$. In the strongest magnetic field regions the quenching reduces the velocity amplitude by $\sim 60\%$, in order to reproduce the magnetic fields ability to quench convective motions in the Sun.

The velocity – scale relation of the driver, averaged over 45 min, is shown in Fig. 2. To illustrate the time development of the driver, snapshots of corks flowing in the time-dependent velocity field produce by the driver are shown in Fig. 3.

2.4. Initial conditions

Two initial stratifications were used. The first was taken from the FAL-C model (Fontenla et al. 1993) in the photosphere, chromosphere and transition region, while in the corona a simple isothermal profile with $T = 10^6$ K was used (see Fig.4). The second was inspired by the work of Carlsson & Stein (see for instance Carlsson & Stein 2002), who argue for a highly time dependent, low mean temperature chromosphere with no average temperature increase. This model has been criticised by Kalkofen (2001), who argues for a warmer chromosphere. On the other hand observations of CO by Ayres (2002) point towards an even cooler chromosphere than the one proposed by Carlsson & Stein. The choice of chromospheric model turns out to have only a minor effect on the coronal dynamics and the coronal heating.

To keep the number of free parameters at a minimum we chose to make the initial magnetic field a potential extrapolation of an observed active region on the Sun. We chose to scale down a high-resolution SOHO/MDI observation of active region 9114 from August 8, 2000. The cropped data spans 500×500 pixels corresponding to roughly 225×225 Mm and was therefore scaled down to fit in the computational box of 60×60 Mm. The dis-

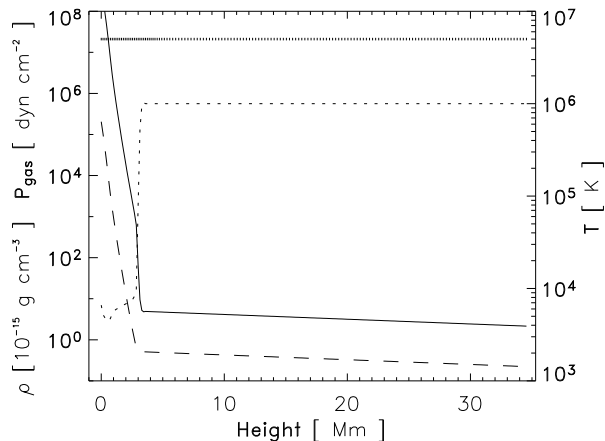


FIG. 4.— Initial stratification for density (full), gas pressure (dashed) and temperature (dotted). Also shown at the top is the vertical-scale, with a small line at each grid point

tribution of flux on the solar surface seems to be approximately self-similar down to scales $\sim 180 \text{ km}$ in the network (Schrijver et al. 1997b; Wang et al. 1995), smaller than our resolution. If this also holds in active regions, as seems to be the case (Meunier 2003), this would justify our “rescaling” of the MDI magnetogram. It is however necessary to point out that our computational box does not hold an average size solar active region, but at most a small active region, and therefore direct comparisons of these results with larger size active regions should be done with care.

3. RESULTS

The simulation goes through a roughly five minute start-up period, where neither thermal conduction nor radiative cooling are turned on. This is related to the magnetic field initial condition. Since the initial magnetic field is potential it is in a minimum energy state and is therefore initially not able to dissipate any energy. In the first few minutes, thermal conduction and radiative cooling would therefore cool the corona monotonically, and make the atmosphere tend to collapse. After the start-up period, when the magnetic field has reached a dissipative state, the radiative cooling and the thermal conduction is turned on. After another approximately five minutes solar time a statistical equilibrium is reached, with a nearly time independent temperature distribution.

3.1. Energy Balance

The thermodynamic equilibrium of the atmosphere is difficult to quantify since the energy fluxes are very intermittent, but several conclusions can still be drawn from a horizontal average of the energy flux divergences, i.e. the deposited energy. The energy balance is shown in Fig. 5. This balance is for a typical point in time, and it is obvious that the heating in the corona is decreasing with height, as found from TRACE data by a number of authors (Schrijver et al. 1999; Aschwanden et al. 2000a, 2001). The detailed height dependence of the heating in individual loops is investigated in a separate paper (Gudiksen & Nordlund 2004).

It is noteworthy and interesting that the convective

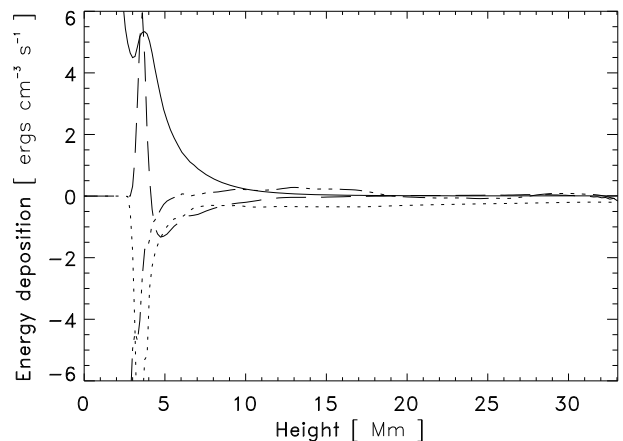


FIG. 5.— Horizontally averaged energy deposition from resistive dissipation (full), Spitzer conductivity (long dash), convective flux (dash dotted) and radiative cooling (dotted), as a function of height

flux redistributes as much energy as the Spitzer conductivity does just above the transition region. The heating provided by the magnetic dissipation is transported by the Spitzer conductivity downwards from the transition region to the upper chromosphere, where the Spitzer conductivity is no longer effective due to the low temperature. The convective flux removes energy at the same location because of evaporation of chromospheric material into the corona. The energy loss in the lower corona and transition zone due to the Spitzer conductivity is balanced by the heating, which dominates the Spitzer conductivity at larger heights. The optically thin radiative losses go to zero in the lower chromosphere and photosphere due to the quenched radiative cooling function that we adopt. The heating goes to very high values, but in spite of that the temperature stays at chromospheric temperatures due to the Newtonian cooling with which we represent the complex chromospheric radiation losses at these height. It is not possible to estimate whether any further heating is needed in the chromosphere until we can consistently treat both convective and radiative energy fluxes through the lower boundary, as well as radiative losses in the optically thick lower atmosphere. There should be no major effect on the conclusions drawn about the heating of the transition region and corona due to this inadequacy, because we hold the temperature structure in this region of the Sun close to what it is deduced to be observationally. Incorporating both enthalpy flux and an appropriate treatment of radiation in a near ab-initio chromospheric model will take a considerable effort, and is a challenge for the future.

3.2. Magnetic field configuration and the dissipative heating

The energy supplied to the corona originates from the Poynting flux through the lower boundary. In general, magnetic dissipative heating is generated from stressing of the magnetic field. The stressing is largest in the photosphere and low chromosphere, where the plasma β is larger than or of the order of unity in a significant fraction of the volume. At these low heights the magnetic field still has a very intermittent structure, reflecting the intermittent distribution set up by fluid motions

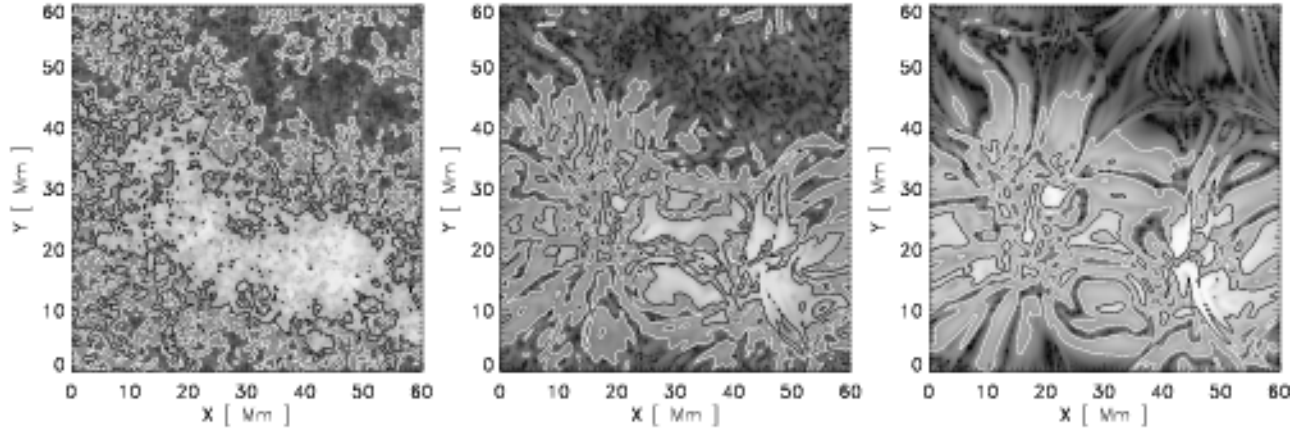


FIG. 6.— Images of the scalar product of electric current and the magnetic field, for three different heights in the atmosphere, 0.0 Mm, 3.0 Mm and 5.6 Mm corresponding to photosphere, upper chromosphere and low corona (left to right). On top are two contours with values a factor of ten apart (black: high, white: low)

in the photosphere and below (represented by the initial and boundary conditions in our numerical model). The plasma β is low in regions with high magnetic field strengths, but is still high in intervening regions with low magnetic field strengths.

In the high chromosphere and above the magnetic field is nearly space-filling and the plasma β is less than unity almost everywhere (with the exception of small neighbourhoods around magnetic null points). The magnetic field thus dominates the dynamics and tends to be ‘nearly force-free’, in the sense that the Lorentz force is small and the electric currents tend to be nearly parallel with the magnetic field,

$$\vec{J} \approx \alpha \vec{B}. \quad (13)$$

As is well known and easily proven, α must be constant along each magnetic field line in a truly force-free field, but can certainly vary from one field line to another. Also, since a dynamically evolving coronal magnetic field cannot be entirely force-free, α should not be expected to be exactly constant even along magnetic field lines.

In order to illustrate the variability of α over horizontal planes, Fig. 6 shows images of the quantity $|\vec{J} \cdot \vec{B}| \approx \alpha B^2$ (we prefer to show this quantity rather than $|\vec{J} \cdot \vec{B}/B^2|$, which would tend to be dominated by regions with low B).

If α was constant these images would effectively be the same as images of B^2 . The actual images show that α varies significantly over horizontal planes, that it varies most rapidly at low heights, and that it certainly cannot be approximated with a constant at any height. The larger horizontal scale of the variability at larger heights is due to the fact that field lines (along which α is at least approximately constant) fan out as they reach higher, and hence spread the variability of α over larger patches.

We next comment on the absolute magnitude of α , and its consequences for the overall field distribution. Dimensionally, α is an inverse length; the length along a field line over which it twists around itself. As previously established by Galsgaard & Nordlund (1996), field lines that are stressed by a boundary typically are twisted only about once from end to end, corresponding to values of α of the order of $1/L$, where L is the field line length.

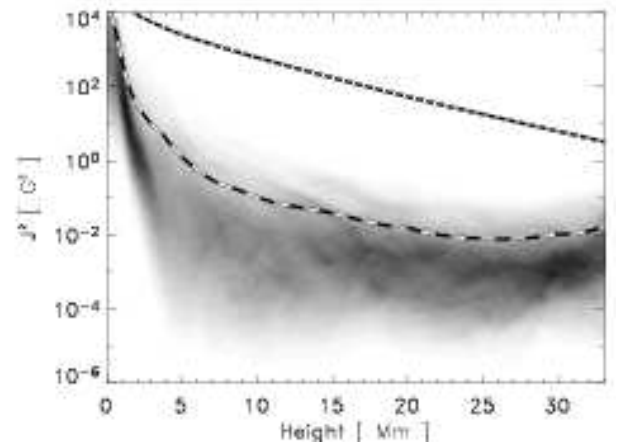


FIG. 7.— PDF of the electric current squared as a function of height, dark colours mean higher PDF with logarithmic colour table. Over-plotted is the horizontal average of the magnetic field squared (dotted) and the horizontal average of the current squared (dashed)

As illustrated by Fig. 6, α is only correlated over small patches near the lower boundary. This implies that the perturbations of the magnetic field line directions must be small (except in special regions such as in the neighbourhood of quasi-separatrix layers (Priest & Démoulin 1995)), and hence that the overall perturbations of the magnetic field strength distribution, relative to that of a potential field, must also be small. This means that to obtain an overall picture of the magnetic field strength distribution, a potential field extrapolation is sufficient in cases like this one, with no large scale shear.

We expect the heating to generally be proportional to the electric current squared and if the field is in a non-linear force free state we also expect the electric current squared and thus the heating to be proportional to the magnetic field strength squared. Figure 7 shows a contour plot of the distribution of heating with height in the atmosphere. One can see that the heating is largest at low heights due to the stressing of the magnetic field in a high β environment. Through the photosphere and

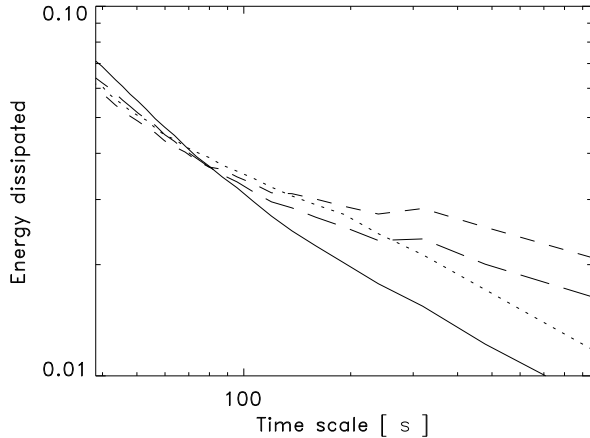


FIG. 8.— Dissipated energy as function of time scale in the upper chromosphere (full), transition region (long dashes), lower corona (dashes) and upper corona (dotted) in arbitrary units. The curves are normalised at the maximum time scale

chromosphere it declines by some four orders of magnitude before reaching the transition region, above which the magnetic field is nearly force free and the heating is indeed approximately proportional to the magnetic field strength squared. Even though the electric current is highly intermittent in horizontal planes, the current relative to the magnetic field strength is almost constant along field lines above the transition region, as is to be expected when α is constant along magnetic field lines. Heating with these characteristics was proposed by Schrijver et al. (1999) and later deduced with data from TRACE by Aschwanden et al. (2001). Further studies of heating models and observations have all supported these heating function characteristics (Mandrini et al. 2000; Foley et al. 2002; Schrijver & Aschwanden 2002; Démoulin et al. 2003; Schmieder et al. 2003).

The time variability of the heating depends critically on height. Figure 8 shows on which time scales the energy dissipation varies, calculated as $k_t \sqrt{P_e}$ where k_t is the time-wavenumber, and P_e is the power spectrum of the dissipated energy as a function of time at each point. This produces a plot showing on what timescales the energy is dissipated. The energy dissipated is normalised to the total amount of dissipated energy. Without this normalisation the curves would be widely spaced along the y-axis, due to the exponential decrease in total dissipated energy with height. In general most of the energy is dissipated as short time scale events. In the upper chromosphere, the energy comes primarily from events with a time scale shorter than the time resolution of our snapshot data set (~ 38 s). Slightly further up into the corona, the fraction of energy dissipated at short time scales is less pronounced. The rapid events most likely correspond to “nano-flare” like reconnection events. With increasing spatial resolution, we would expect to resolve smaller and smaller and hence increasingly more short-lived events.

The energy supplied by the Poynting flux is distributed initially between changes of kinetic, thermal, potential and magnetic energy, and dissipation. After the system has settled into a statistical equilibrium the energy is only used to compensate for magnetic and kinetic dis-

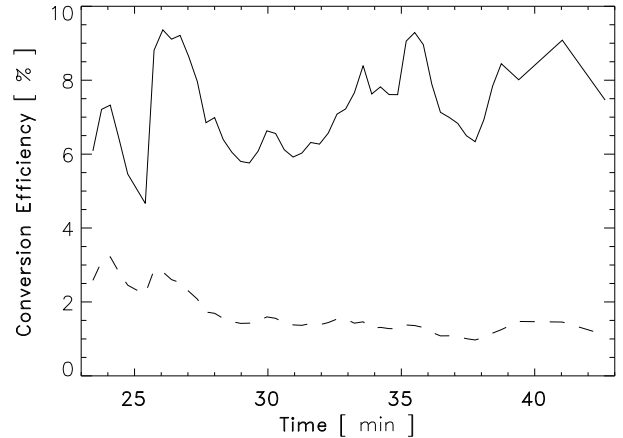


FIG. 9.— Energy conversion efficiency as function of time during a 23 min period. The relative amount of energy converted into heating (solid) and the relative amount of energy lost to radiation (dashed) in the corona are shown

sipation. The energy is dissipated in the whole atmosphere, with the main part in the photosphere and chromosphere. The Poynting flux at the lower boundary is highly intermittent but the total Poynting flux is close to constant. Comparing the flux of energy through the lower boundary and the heating rate in the corona gives an overall energy conversion “efficiency”. The time evolution of the efficiency is shown in Fig. 9(solid) during a 20 min period. During this time the numerical resistivity was changed several times, apparently without significant effect on the efficiency. The efficiency is in the range 5–10 %. That the changes in resistivity have little effect both on the Poynting flux into the system and on the efficiency also confirms the results of Hendrix et al. (1996) and Galsgaard & Nordlund (1996). The radiative losses of the corona is in the range 1–3 % during the same time period (Fig. 9, dashed) making it less important than the Spitzer conductivity, as expected.

The total amount of heating needed in active regions has been estimated several times based on UV and X-ray fluxes, and typically gives values in the range 10^6 – 10^7 ergs $\text{cm}^{-2} \text{s}^{-1}$. These values are in general hard to estimate precisely, since the total area of the active region can be chosen based on different criteria. Figure 10 shows the average dissipated energy per second and square centimetre in our model, in gas that is emitting UV and X-rays ($T > 5 \times 10^5$ K), in volumes below which the photospheric magnetic field is higher than a certain threshold. If only regions with high magnetic field strength below them are taken into account the average energy dissipation can be as high as 8×10^6 ergs $\text{cm}^{-2} \text{s}^{-1}$, while if one includes areas with lower field strengths the average dissipation rate declines, but remains above 2×10^6 ergs $\text{cm}^{-2} \text{s}^{-1}$ for the field strengths shown in Fig. 10. These values of the average heating are well within the observational limits. The total energy dissipated if the chromosphere and transition region are also included is substantially larger than these numbers, because most of the energy is dissipated in the high field strength environment of the lower atmosphere.

3.3. Stratification

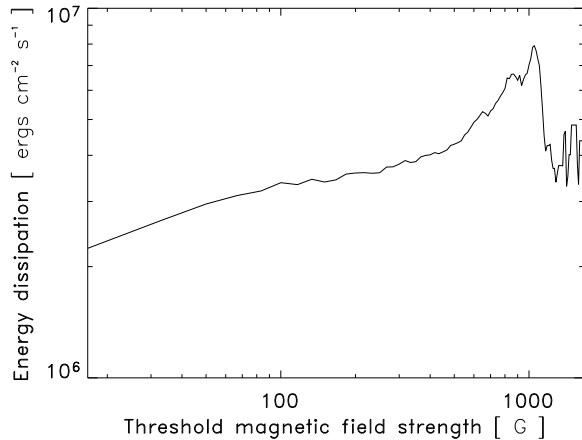


FIG. 10.— Average heating rate in UV to X-ray emitting gas as a function of the underlying photospheric magnetic field strength threshold

As limb observations by TRACE have indicated for some time (Schrijver & McMullen 1999; Title & Schrijver 2003, private communication), the transition region does not occur at a well defined height. The variation in transition region height, defined in our model as the height where the temperature rises above 10^5 K, is shown in Fig. 11 for one of the snapshots. The height above the photosphere varies from 2.7 Mm to 12.3 Mm, with an average of 5.0 Mm, and changes over small distances. The intermittency of the height of the transition region is a result of the intermittent heating, which causes evaporation and re-condensation of chromospheric material.

The stratification of the corona is intermittent on even the smallest scales. The temperature is generally around 1 MK but there are large deviations from this average temperature. There are differences in temperature of up to 0.7 MK over distances comparable to TRACE's pixel size (~ 375 km). The temperature gradients are most likely limited by the numerical resolution and are therefore only lower limits. Because of the large temperature gradients, modelling coronal loops as monolithic structures cannot be a good approximation, thus making multi-thread models of loops called for (Aschwanden et al. 2000b).

Figure 12 shows that even at large heights in the corona there is gas at low temperatures. Evidence for cool gas suspended in the corona has been found through limb observations with TRACE based on opacity estimates (Schrijver & McMullen 1999; Schrijver et al. 1999). The cool dense material in the lower part of the corona are primarily surges of chromospheric material that flow into the corona, or condensations of coronal material on its way down. Higher up in the corona it is typically gas undergoing catastrophic cooling (Schrijver 2001). At times surges of material happen simultaneously in both foot points of a loop, which brings large amounts of material to the top of the loop. If the loop is inclined relative to the vertical, accumulated mass at its top can force the loop top down and make it almost horizontal along part of its length, thus suspending the cold material in the corona. An example is the large structure at roughly $(x, y) = (40, 25)$ in Fig. 11, which has a horizontal col-

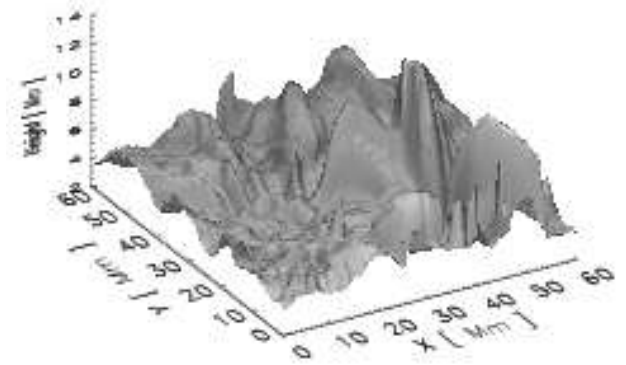


FIG. 11.— Surface showing the height of the transition region, defined as where the temperature rises above 10^5 K

umn density of up to $6 \times 10^{20} \text{ cm}^{-2}$ at a height of 8.0 Mm, making it a visible absorbing structure for UV at the limb. The structure is long lived, having existed for 10 minutes at the end of the simulation sequence. There are other similar structures, but too few to give a basis for firm estimates of typical characteristics.

The density has values that vary by at least 2 orders of magnitude in the corona, over any horizontal slice. The average density and temperature in the corona depend primarily on the amount of Poynting flux injected through the lower boundary and on the choice of the chromospheric temperature structure, while the horizontal variations of density and temperature primarily reflect the variations of properties from loop to loop. In general the highest densities are in loop structures with low temperatures, persisting all the way to the top of the atmosphere. A 2D histogram of the Probability Density Function (PDF) of the density at each height for the FAL-C chromosphere is displayed in Fig. 13, which shows that the horizontally averaged density stays almost constant through the part of the corona that we model, with an average number density close to 10^9 cm^{-3} , but with values ranging from 10^8 to a few times 10^{10} cm^{-3} , typical of or slightly higher than observed for active regions loops (see for instance Mason et al. 1999).

The velocities in the corona are not completely field aligned. In the lower corona 80 % of the velocity amplitude is along the magnetic field, whereas higher in the corona the fraction drops to roughly 50 %. In the lower corona the strong field regions have velocities that are almost fully field aligned, while the lower field strength regions have less prevalence for velocities along the magnetic field. In the upper corona the velocities are no longer strongly correlated with the magnetic field, and the velocities perpendicular to the magnetic field are now as strong as those aligned with the magnetic field. In general the velocity amplitudes in the corona are highest just above the transition region, where the impulsive energy releases can accelerate plasma to high velocities. Velocities in this region reach as high as 400 km s^{-1} but with an average of only a few tens of km s^{-1} .

3.4. TRACE emission measure

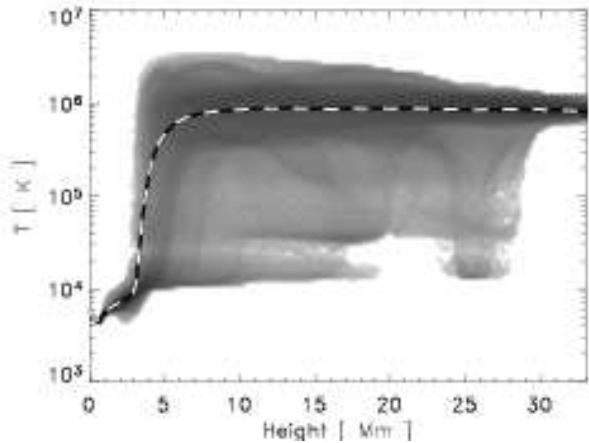


FIG. 12.— Histogram of the temperature PDF for each height for the FAL-C chromosphere. Dark is high PDF, with a logarithmic grey scale. The horizontal average is over plotted (dashed)

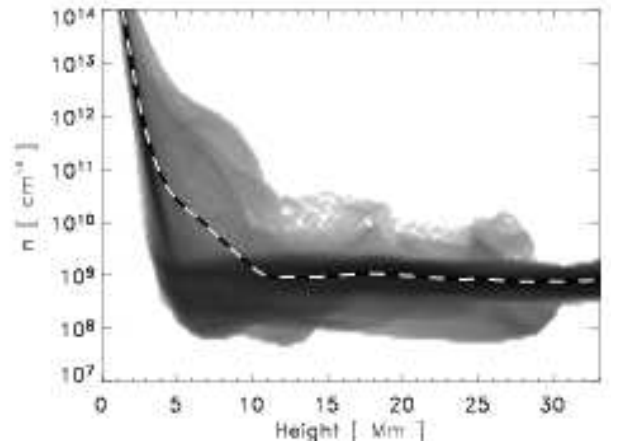


FIG. 13.— Histogram of the density PDF for each height for the FAL-C chromosphere. Dark is high PDF, with a logarithmic grey scale. The horizontal average for the distribution is over plotted (dashed)

Direct comparison of actual photon count rates between TRACE observations and these simulations is complicated for several reasons. Del Zanna & Mason (2003) pointed out that the temperature response functions of the TRACE filters are based on the Chianti v2.0 database (Landi et al. 1999), which does not include recombinations to and transitions for Fe VIII, and this affects the response functions somewhat. Several ionisation equilibria models are published (see for instance Mazzotta et al. 1998; Arnaud & Raymond 1992; Arnaud & Rothenflug 1985), with differences that can give changes in the response function by up to a factor of two (Del Zanna & Mason 2003, private communication). In this work, we have used the TRACE response function found by Del Zanna & Mason (2003), with the ionisation states of Mazzotta et al. (1998) and the elemental abundances by Feldman (1992), calculated at a constant electron pressure of $10^{15} \text{ K cm}^{-2}$. We have also made calculations using the local electron pressure instead of a constant electron pressure, and found that the difference is minor (typically less than 10 %), but the calculations are much more computationally expensive.

The images in Fig. 14 have been produced by folding the temperatures and densities of the simulation with the response function. In the run with the FAL-C chromosphere the calculated intensities in the TRACE 171 and 195 filters are between 60-70 and 15-25 $\text{DN s}^{-1} \text{ pixel}^{-1}$. For individual loops chosen from the emulated TRACE 171 image, that is too high by almost a factor ten for the 171 filter and a factor 3 for the 195 filter compared to the values given by Del Zanna & Mason (2003). There are several possible explanations for this discrepancy. The images show a forest of loops of all heights. Some of the loops appear broad and diffuse but this is often an effect of the perspective—most of these broad loops are not connected along the projected axis. The numbers in Del Zanna & Mason (2003) are for a single, well isolated high reaching loop while the large number of loops in the emulated images often are hard to isolate. The maximum coronal loop height in the current model is limited to $\sim 30 \text{ Mm}$; loops penetrating the upper boundary are not reliable, since the boundary conditions cannot rigorously model the effects of the loop top on the part of the

loop included in the box. The count rates are therefore hard to compare directly. The difference in the count rates in the two filters indicates that there is lack of high temperature material. Based on the previous work by Galsgaard & Nordlund (1996), we expect that higher resolution will create more intermittent structures, creating a broader range of temperatures and effectively shifting gas out of the 171 and 195 filters.

Cross sections and other properties for individual loops are examined in a separate paper (Gudiksen & Nordlund 2004).

4. CONCLUSION

The increase in computer performance and system memory in recent years has made it possible to approach the solar coronal heating problem from a new angle. Previously mainly qualitative models have been developed, with assumptions of the magnetic field structure and/or the atmospheric stratification that necessarily have been simplified. This has kept conclusions about the underlying processes indecisive. In recent years observational results coming from the SOHO and TRACE satellites have been able to put constraints on the overall heating function, favouring a heating function decreasing exponentially with height (Schrijver et al. 1999; Aschwanden et al. 2000a, 2001). Observations of nano- and micro-flares seem to indicate that even if one extrapolates the distributions down to energies which are unobservable, they are not able to supply all the energy needed (Aschwanden & Charbonneau 2002; Aschwanden & Parnell 2002; Parnell & Jupp 2000).

By performing direct numerical simulations we have been able to show that moving foot points of the magnetic field around in a way consistent with the observed solar photospheric velocity fields inevitably leads to an amount of energy dissipation in the corona that is comfortably within the observational limits. The approach is nearly *ab initio*, using only observed facts such as the average velocity field properties, a realistic active region photospheric magnetic field, a realistic optically thin cooling function, Spitzer conductivity, etc.

As anticipated by Parker (1972), and as demon-

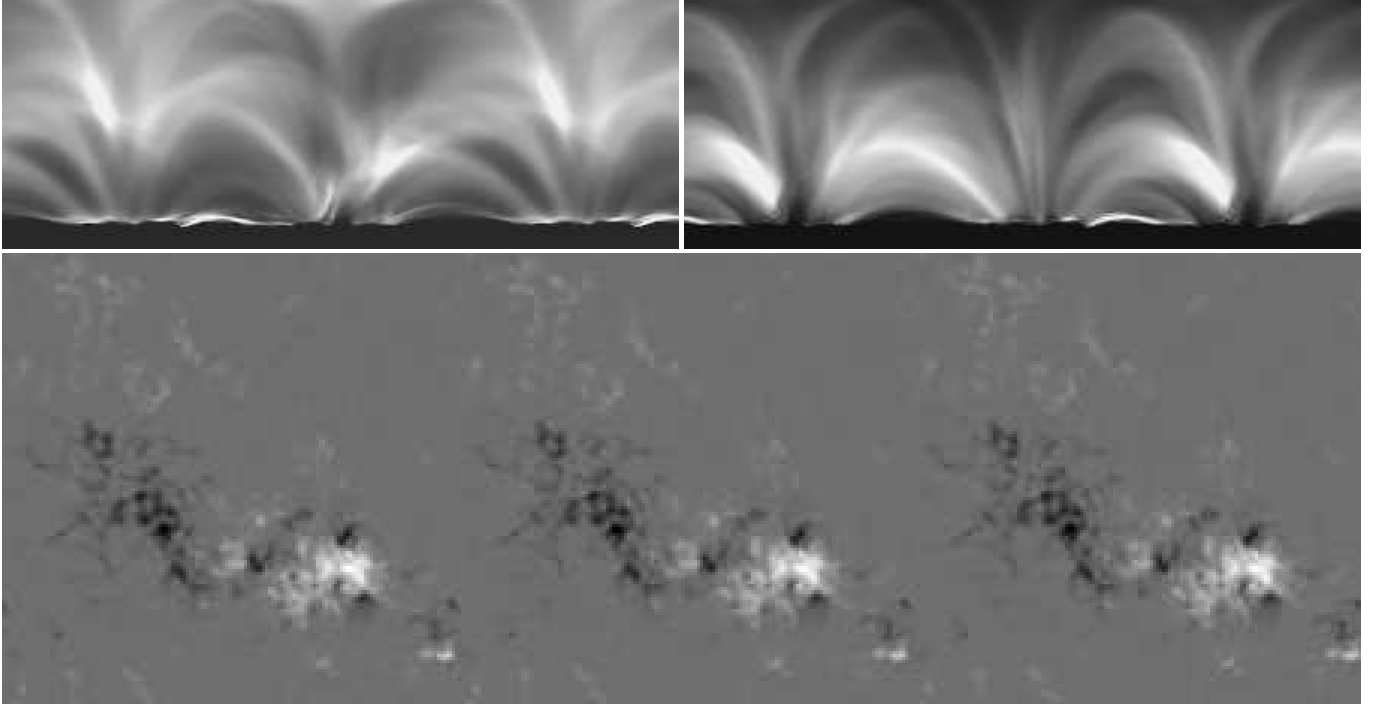


FIG. 14.— Emulated TRACE 171 (left top) and 195 (right top) images both spanning 1.5 box lengths, and the underlying photospheric magnetic field

strated numerically by Galsgaard & Nordlund (1996) and Hendrix et al. (1996), the magnetic dissipation is expected to depend only weakly on the numerical resolution. If anything it *increases* slightly as smaller scales are resolved. An aspect that *will* depend on numerical resolution, however, is the time variability and intermittency of the heating. As demonstrated by Galsgaard & Nordlund (1996), the hierarchy of current sheets in which the magnetic dissipation takes place extends to ever smaller size as the numerical resolution is increased. It is presumably the intrinsic time variability from the reconnection events in this hierarchy that gives rise to the flare event size power law distribution. From this point of view, there is no conflict between the current model and the observations that have inspired the nano-flare coronal heating models.

The main results of the coronal modelling is that the total dissipated energy is within the observational limits, making this heating mechanism at least a major constituent (and an unavoidable one!) in heating the solar corona. The energy release should at least partially be observable as a distribution of flare-like events (Galsgaard & Nordlund 1996), but we cannot yet estimate the fraction of the energy released in the form of nano-flares, or predict their energy distribution, since this requires very high numerical resolution, outside the range of present day computer capabilities.

The magnetic field is in two distinctly different states above and below the height where the $\beta = 1$ layer is located. Below, the field is controlled by the photospheric gas motions, and is in general in a non-relaxed state. The magnetic field there dissipates energy at a high rate, since the magnetic energy density is high, the magnetic field lines are short, and since oppositely directed field lines

may be forced towards each other without the magnetic pressure having a significant effect on the total pressure.

In the present simulations roughly 90 % of the total dissipated energy is dissipated below the transition region. Above the transition region the magnetic field assumes a non-linear near-force-free configuration, where the dissipated energy is roughly proportional to the magnetic energy density. Several observations point towards a heating function with precisely these properties (Mandrini et al. 2000; Foley et al. 2002; Schrijver & Aschwanden 2002; Démoulin et al. 2003; Schmieder et al. 2003).

The results for the distribution of both temperature and density are also well within the observed values, even though these values might change slightly depending on the stratification of the upper chromosphere. The temperature is intermittent on the smallest scales, changing by as much as 0.7 MK on the scale of a TRACE pixel size. The temperature has values from 10^4 to 3×10^6 K in most of the corona, with a transition zone defined as being at temperatures near 5×10^5 K varying by as much as 9 Mm in height, similar to what has been inferred from TRACE observations (Schrijver & McMullen 1999; Title & Schrijver 2003, private communication). The average density is almost constant with height in the corona, but has values at each height spanning two orders of magnitude.

From the point of view of the energy balance, the density and temperature in the corona play different but tightly coupled roles. On the one hand the radiative cooling function changes relatively little with temperature, from a few times 10^5 K to a few times 10^6 K, while the cooling per unit volume is proportional to the square of the density. On the other hand heat conduc-

tion scales as $T^{7/2}$, but any increase in heat conduction also results in more evaporation from the chromosphere, so tends to increase the density in the corona. So in this sense the temperature is not by itself a sensitive probe for the heating in the corona, but has to be taken together with density information, and with information about the temperature gradients along the magnetic field.

Making a direct comparison with TRACE observations of an active region is hampered by both the question of the statistical significance of a single observation, and by the insufficient knowledge of the ionisation balance in the corona which makes computed photon count rates uncertain by up to a factor of two. Furthermore, the density in the corona is a function of the stratification in the chromosphere, as commented upon earlier.

In spite of these difficulties the emission measures in the TRACE 171 and 195 Å bands estimated from the simulations are not far from observed values. The discrepancies (mainly too much emission in the 171 band) is most likely due to missing intermittency, in turn due to the limited numerical resolution. As discussed in the previous Section, increased numerical resolution is expected to give a broader distribution of temperatures, reaching higher peak values. This will reduce the emission measure in the 171 band and will also affect the 195 band.

To reproduce the hotter Yohkoh-loops will certainly require a temperature distribution that extends to higher values than what we find here. Increased heating will inevitably result if a more complete representation of the solar velocity field is used. In the current simulations there is a resolution cut-off in the velocity driving towards smaller scales, and a box size cut-off towards larger scales. It is interesting to note that scaling expressions

for coronal heating predict that the heating should scale with the product of the velocity amplitude and the size scale of the motions, so there should be significant additional heating from larger scales. However, with the turn-over time varying roughly as the square of the scale of motions, it will take an ever increasing amount of computer capacity to recover these contributions from larger scale motions.

A more accessible but less well defined contributor to additional heating would be active-region-specific velocity fields, such as shearing motions, sunspot rotation, etc.. Such systematic motions would cause systematically stressed magnetic fields, producing locally enhanced heating rates in areas affected by the additional systematic motions. Emerging flux is another contributor to heating that is not treated in this simulation but happens continuously on the Sun and will produce additional heating if included.

BVG acknowledges support through an EC-TMR grant to the European Solar Magnetometry Network. The work of ÅN was supported in part by the Danish Research Foundation, through its establishment of the Theoretical Astrophysics Center. Computing time was provided by the Swedish National Allocations Committee and by the Danish Center for Scientific Computing. The authors thank G. Del Zanna for the improved TRACE response function, R. Nightingale for general help with the TRACE characteristics and V. Hansteen for providing the radiative cooling function. Both authors gratefully acknowledge the hospitality of LMSAL and ITP/UCSB (through NSF grant No. PHY99-07949) during this work.

REFERENCES

- Alfvén, H. 1947, MNRAS, 107, 211
 Arnaud, M. & Raymond, J. 1992, ApJ, 398, 394
 Arnaud, M. & Rothenflug, R. 1985, A&AS, 60, 425
 Aschwanden, M. J. 1987, Sol. Phys., 111, 113
 Aschwanden, M. J. & Charbonneau, P. 2002, ApJ, 566, L59
 Aschwanden, M. J., Nightingale, R. W., & Alexander, D. 2000a, ApJ, 541, 1059
 Aschwanden, M. J., Nightingale, R. W., & Alexander, D. 2000b, ApJ, 541, 1059
 Aschwanden, M. J. & Parnell, C. E. 2002, ApJ, 572, 1048
 Aschwanden, M. J., Schrijver, C. J., & Alexander, D. 2001, ApJ, 550, 1036
 Aschwanden, M. J., Tarbell, T. D., Nightingale, R. W., et al. 2000, ApJ, 535, 1047
 Ayres, T. R. 2002, ApJ, 575, 1104
 Bondi, H., Hoyle, F., & Lyttleton, R. A. 1947, MNRAS, 107, 184
 Carlsson, M. & Stein, R. F. 2002, ApJ, 572, 626
 Davila, J. M. 1987, ApJ, 317, 514
 Del Zanna, G. & Mason, H. E. 2003, A&A, 406, 1089
 Démoulin, P., van Driel-Gesztelyi, L., Mandrini, C. H., Klimchuk, J. A., & Harra, L. 2003, ApJ, 586, 592
 Dorc, S. B. F., Archontis, V., & Nordlund, Å. 1999, A&A, 352, L79
 Dorc, S. B. F. & Nordlund, A. 1998, A&A, 338, 329
 Feldman, U. 1992, Physica Scripta Volume T, 46, 202
 Foley, C. R., Patsourakos, S., Culhane, J. L., & MacKay, D. 2002, A&A, 381, 1049
 Fontenla, J. M., Avrett, E. H., & Loeser, R. 1993, ApJ, 406, 319
 Galsgaard, K. & Nordlund, Å. 1996, J. Geophys. Res., 101, 13445
 Glencross, W. M., Dorling, E. B., & Herring, J. R. H. 1974, Sol. Phys., 38, 183
 Gomez, D. O., Dmitruk, P. A., & Milano, L. J. 2000, Sol. Phys., 195, 299
 Gudiksen, B. V. & Nordlund, Å. 2002, ApJ, 572, L113
 Gudiksen, B. V. & Nordlund, Å. 2004, ApJ, submitted
 Hathaway, D. H., Beck, J. G., Bogart, R. S., et al. 2000, Sol. Phys., 193, 299
 Hendrix, D. L., van Hoven, G., Mikic, Z., & Schnack, D. D. 1996, ApJ, 470, 1192
 Heyvaerts, J. & Priest, E. R. 1983, A&A, 117, 220
 Heyvaerts, J. & Priest, E. R. 1992, ApJ, 390, 297
 Judge, P. G. & Meisner, R. 1994, in The Third Soho Workshop, Solar Dynamic Phenomena and Solar Wind Consequences, ed. J. J. Hunt (ESTEC, Noordwijk, the Netherlands: ESA SP-373), 67–71
 Kalkofen, W. 2001, ApJ, 557, 376
 Landi, E., Landini, M., Dere, K. P., Young, P. R., & Mason, H. E. 1999, A&AS, 135, 339
 Longcope, D. W. & Sudan, R. N. 1994, ApJ, 437, 491
 Mandrini, C. H., Démoulin, P., & Klimchuk, J. A. 2000, ApJ, 530, 999
 Mason, H. E., Landi, E., Pike, C. D., & Young, P. R. 1999, Sol. Phys., 189, 129
 Mazzotta, P., Mazzitelli, G., Colafrancesco, S., & Vittorio, N. 1998, A&AS, 133, 403
 Meunier, N. 2003, A&A, 405, 1107
 Mikic, Z., Schnack, D. D., & van Hoven, G. 1989, ApJ, 338, 1148
 Neubauer, F. M. & Musmann, G. 1977, J. Geophys. Res., 82, 3201
 Nordlund, Å., Galsgaard, K., & Stein, R. F. 1994, in NATO ASI Series, Vol. 433, Solar Surface Magnetic Fields, ed. R. J. Rutten & C. J. Schrijver (Dordrecht: Kluwer)
 Ofman, L. & Davila, J. M. 1997, ApJ, 476, L51
 Okabe, A., Boots, B., & Shugihara, K. 1992, Spatial Tessellations: Concepts and Applications of Voronoi Diagrams (Chichester: Wiley)
 Padoan, P. & Nordlund, Å. 1999, ApJ, 526, 279
 Parker, E. N. 1972, ApJ, 174, 499

- Parker, E. N. 1979, *Cosmical magnetic fields: Their origin and their activity* (Oxford, Clarendon Press; New York, Oxford University Press)
- Parker, E. N. 1983, *ApJ*, 264, 642
- Parnell, C. E. & Jupp, P. E. 2000, *ApJ*, 529, 554
- Priest, E. R. & Démoulin, P. 1995, *J. Geophys. Res.*, 100, 23443
- Schmieder, B., Rust, D., Georgoulis, M., & Bernasconi, P. 2003, in *Stars as Suns: Activity, Evolution and Planets*, Vol. 219, –
- Schrijver, C. J. 2001, *Sol. Phys.*, 198, 325
- Schrijver, C. J. & Aschwanden, M. J. 2002, *ApJ*, 566, 1147
- Schrijver, C. J., Hagenaar, H. J., & Title, A. M. 1997a, *ApJ*, 475, 328
- Schrijver, C. J. & McMullen, R. A. 1999, *Bulletin of the American Astronomical Society*, 31, 964
- Schrijver, C. J., Title, A. M., Berger, T. E., et al. 1999, *Sol. Phys.*, 187, 261
- Schrijver, C. J., Title, A. M., van Ballegoijen, A. A., Hagenaar, H. J., & Shine, R. A. 1997b, *ApJ*, 487, 424
- Shine, R. A., Simon, G. W., & Hurlburt, N. E. 2000, *Sol. Phys.*, 193, 313
- Shull, J. M. & van Steenberg, M. 1982, *ApJS*, 48, 95
- Simon, G. W. & Weiss, N. O. 1968, *Zeitschrift fur Astrophysics*, 69, 435
- Simon, G. W. & Weiss, N. O. 1989, *ApJ*, 345, 1060
- Spitzer, L. 1956, *Physics of Fully Ionized Gases* (New York: Interscience)
- Stein, R. F. & Nordlund, A. 1998, *ApJ*, 499, 914
- Sturrock, P. A. & Uchida, Y. 1981, *ApJ*, 246, 331
- Title, A. & Schrijver, K. 2003, in *Stars as Suns: Activity, Evolution and Planets*, Vol. 219, –
- van Ballegoijen, A. A. 1986, *ApJ*, 311, 1001
- Wang, J., Wang, H., Tang, F., Lee, J. W., & Zirin, H. 1995, *Sol. Phys.*, 160, 277